Journal of Alloys and Compounds 1038 (2025) 182889

Contents lists available at ScienceDirect

Journal of Alloys and Compounds

journal homepage: www.elsevier.com/locate/jalcom

From ferrimagnetism to spin-glass behavior in alkali- and rare-earth metal crichtonites

Ruiqi Chen [a,b], José Luis Rosas-Huerta [a,c,d,*], Clemens Ritter [e], Claire Minaud [a], Oleg Siidra [b], Marie Colmont [a], Ángel M. Arévalo-López [a,**]

[a] Unité de Catalyse et Chimie du Solide (UCCS) - UMR CNRS 8181, Université de Lille - Centrale Lille, Université Artois, ENSCL, Lille F-59000, France
[b] Department of Crystallography, Institute of Earth Sciences, St. Petersburg State University, University emb. 7/9, St. Petersburg 199034, Russia
[c] Facultad de Ciencias, Universidad Nacional Autónoma de México, AP 70-399, CDMX, 04510, Mexico
[d] Escuela Superior de Ingeniería Mecánica y Eléctrica-Culhuacan, Instituto Politécnico Nacional, Av. Santa Ana 1000, Ciudad de México 04440, Mexico
[e] Institut Laue-Langevin, BP 156, Grenoble Cedex 38042, France

ARTICLE INFO

Keywords:
Magnetic materials
Neutron diffraction
Solid-state synthesis

ABSTRACT

In this work, nine new synthetic alkali- and rare-earth metal crichtonite-type compounds with $AB_3C_{18}O_{38}$ general formula are presented. The effect on the magnetic properties as consequence of the substitution of divalent and trivalent cations in the *A* site, as well as the introduction of iron at the *B* and *C* sites is studied. Ferrimagnetic behavior was identified in the crichtonites $CaMn_3Ti_{18}O_{38}$, $BaMn_3Ti_{18}O_{38}$ and $CaFe_3Ti_{18}O_{38}$, which changes to a spin-glass type for the $BaMn_3Ti_{14}Fe_4O_{38}$ and *A*-trivalent $REMn_3Ti_{18}O_{38}$ (RE = La, Ce and Nd), $LaFe_3Ti_{18}O_{38}$ and $LaMn_3Ti_{13}Fe_5O_{38}$. A comprehensive comparison of the AC and DC magnetic measurements for whole series along with the FiM structure obtained by neutron powder diffraction is discussed. These results will expand the comprehension on this almost unexplored magnetic family of compounds.

Complex oxides can crystallize in a wide variety of structures such as spinel, pyrochlores, perovskites, crichtonites, etc. These contain different atomic species that allow a wide variety of potential applications such as photovoltaics, nuclear waste containers, spintronic, magnetoresistive, superconductors, multiferroic materials, etc [1–3]. Substitution of the different constituents in these materials is the common strategy to fine tune their properties. For instance, in the double perovskites $A_2FeMoO_{6-\delta}$ with A = Ca, Sr and Ba, the mixed valences $Fe^{2+/3+}$-$Mo^{6+/5+}$ changes to mostly Fe^{2+}-Mo^{6+} as the A cation size increases, thus reducing the number of Mo itinerant electrons [4]. This size change also promotes the increase of symmetry from monoclinic to tetragonal and finally cubic for Ca, Sr and Ba, respectively [5]. Furthermore, the substitution of rare-earth (RE) elements in RE_2NiIrO_6 (RE = La, Pr and Nd) results in the enhancement of the Néel temperature (T_N) as the ionic radius decreases and the number of free electrons increases, T_N = 75 K, 103 K and 121 K for La, Pr and Nd, respectively [6].

In this article we focus on the crichtonite-family and following the strategy sketched above, we study substitutions of alkali- and rare-earth metals in their composition and the influence on their magnetic properties. Crichtonites can be represented with the $AB_3C_{18}O_{38}$ general formula. They are a large family of minerals named accordingly to the majority element in the *A* site which can be monovalent, divalent or trivalent elements, like mathiasite (K), davidite (U), loveringite (Ca), lindsleyite (Ba), crichtonite (Sr) and rare earth elements. They have mainly been studied from natural samples, but some have been synthesized via high temperature and pressure, hydrothermal or solid-state techniques [7]. However, until now the main focus of these studies has been on the determination of their composition and structure [8–14]. The synthetic $SrFe_3V_{18}O_{38}$ [15] and $BaMn_3Ti_{18}O_{38}$ [9] were reported containing a V^{3+}/V^{4+} and Ti^{3+}/Ti^{4+} mixed valence state, which inspired our previous study of $SrMn_3Ti_{18}O_{38}$ (SrMTO) and $SrMn_3Ti_{14}Fe_4O_{38}$ (SrMTFO) compounds [16]. In this work, we extend our studies on this relatively unexplored crichtonite family and present nine compounds along with their magnetic properties, crystal and magnetic structures and the rationale of the different substitution effects. The studied compositions are $AMn_3Ti_{18}O_{38}$ with *A* = Ca, Ba, La, Ce and Nd (*A*MTO), $CaFe_3Ti_{18}O_{38}$ (CaFTO), $BaMn_3Ti_{14}Fe_4O_{38}$ (BaMTFO), $LaFe_3Ti_{18}O_{38}$ (LaFTO) and $LaMn_3Ti_{13}Fe_5O_{38}$ (LaMTFO).

* Corresponding author at: Unité de Catalyse et Chimie du Solide (UCCS) - UMR CNRS 8181, Université de Lille - Centrale Lille, Université Artois, ENSCL, Lille F-59000, France.
** Corresponding author.
E-mail addresses: joseluis_rosas@comunidad.unam.mx (J.L. Rosas-Huerta), angel.arevalo-lopez@univ-lille.fr (Á.M. Arévalo-López).

https://doi.org/10.1016/j.jallcom.2025.182889
Received 23 April 2025; Received in revised form 24 July 2025; Accepted 7 August 2025
Available online 8 August 2025

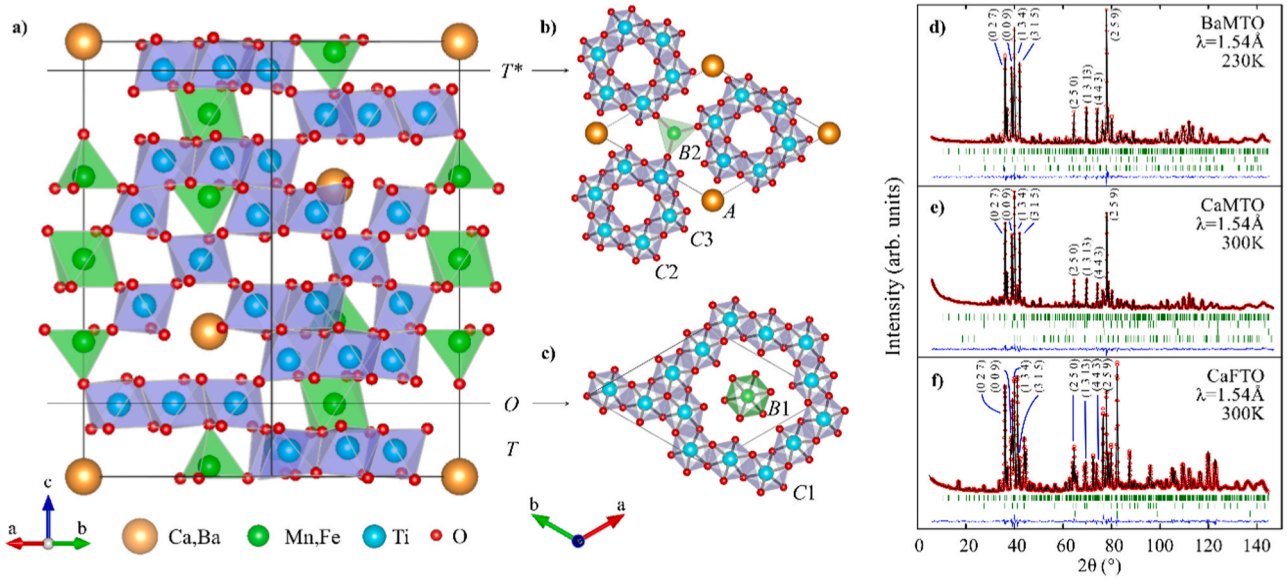

Fig. 1. a) Crystal structure of crichtonite compounds along (110) plane, b) (001) plane at z = 0.9 and c) at z = 0.2. Brown, green, light blue and red balls represent the (Ca,Ba,RE), (Mn,Fe), (Ti,Fe) and O atoms, respectively. NPD Rietveld refinements (λ = 1.54 Å) at room temperature for d) BaMTO, e) CaMTO and f) CaFTO compounds are shown; red empty circles, black and blue lines and vertical bars are the observed data, fitted, difference and Bragg reflections, respectively. Lower tick marks refer to secondary phases detailed in Table S1.

Crichtonites compounds were synthesized through solid-state reaction under vacuum. Chemical reagents (MnO, Ti, TiO_2, MnO_2, Fe, Fe_2O_3, La_2O_3, CeO_2, Nd_2O_3, $CaCO_3$ and $BaCO_3$) with a purity higher than 99.9 % were used in our syntheses. They were mixed in respective stoichiometric ratios to obtain the desired compounds. For the A-site divalent compositions (Ca, Ba), the precursors (Ca,Ba)$Ti_{14}O_{29}$, (Ca,Ba)$Ti_{16.5}O_{34}$ and $CaTi_{11}O_{23}$ were first prepared from reactants stoichiometric mixtures; calcium and barium carbonates and anatase, which were weighed, mixed thoroughly and heated at 900 °C for 12 h in air to decompose the carbonate. As a second step, the reagents, along with decarbonated precursors when needed, were weighed stoichiometrically, mixed thoroughly and pressed into pellets weighing 80 mg. The pellets were placed in vacuum sealed quartz tubes. The synthesis starts with heating to 650 °C at a rate of 5°/min and held for 12 h, the temperature was then increased to 1100 °C at the same rate with a dwell time of 48 h. Finally, it was cooled to room temperature by turning off the furnace.

The purity of synthesized compounds was initially examined by X-ray diffraction (XRD) at room temperature in a Bruker D8 Advance diffractometer with Cu Kα radiation (λ = 1.54 Å), see Fig. S1 and S2 in the Supplementary Information (SI). The crystal and magnetic structures were studied by means of neutron powder diffraction (NPD) carried out at the Institut Laue-Langevin in Grenoble, France (ILL) in the D20 beamline with a λ = 1.54 Å wavelength for high resolution and λ = 2.42 Å for magnetic structure resolution. ISODISTORT was used to determine the possible magnetic structures and space groups [17]. Rietveld refinement analyses and visualizations of the magnetic structure were made through the Fullprof suite and Fullprof Studio software [18,19]. DC and AC magnetic susceptibility and heat capacity measurements were carried out in a Dynacool Physical Property Measurement System (PPMS) from Quantum Design. DC magnetic susceptibility (χ) was measured from 2 to 300 K under zero-field cooling (ZFC) and field cooling (FC) conditions, under 0.1 T external magnetic field. Magnetization (M) as a function of applied magnetic field (H) was measured from −9 to 9 T at different temperatures. AC-magnetic susceptibility was measured at different frequencies with an oscillating ±16 Oe magnetic field. Heat capacity measurements were made by the relaxation method.

Besides the $AB_3C_{18}O_{38}$ crichtonite general formula, the crystal structure can be better described by the formula $^{XII}A1^{VI}B1^{IV}B2_2^{VI}C1_6^{VI}C2_6^{VI}C3_6O_{38}$ where *A*, *B* and *C* sites stand for six different metal positions where the oxygen coordination is indicated by the left roman numeral exponent. The dodecahedron *A*1-site is the largest and it is normally occupied by a divalent or trivalent cation, while *B* and *C* sites are occupied by transition metals [20,21]. The structure is built by a rhombohedral sequence of three layers $(TOT^*)_3$ in the *R-3* space group. The *T* layer is composed by *C*1 and *C*2 octahedra sharing edges creating hexagonal rings linked by the *B*2 tetrahedra and *A*1, layers *T** and *T* are related via an inversion center as shown in Fig. 1. *O* layer is composed by twelve *C*3 octahedra creating a larger hexagonal arrangement with the *B*1 octahedron at the center. The connection between *T* and *O* layers is only through vertices while inside *T* and *T** layers is through *C* edges. Main crystallographic data obtained by Rietveld refinements analyses are shown in Table 1, S1, S2 and S3 for the nine different compounds studied in this work. High resolution NPD representative Rietveld refinement fits are shown in Fig. 1 for BaMTO, CaMTO and CaFTO, remaining fits are given in Fig. S1 and S2.

Rietveld refinements indicate that all the synthesized crihtonites crystalize in the rhombohedral *R-3* space group, some secondary phases were also identified as detailed in SI with TiO_2 being the most common one. When comparing the cell parameters for the A-site divalent CaMTO and BaMTO, an unexpected larger *a* parameter is observed for the former. This is due to 0.15 Mn by Ca partial substitution in the *B*1 site and Ca ionic radii in octahedral coordination being larger than Mn (1.00 *vs.* 0.83 Å for Ca and Mn respectively). This mixed site occupation has also been reported in $Ca_{1.5}Mn_{1.8}Ti_{18.7}O_{38}$ or $Ca_2Zn_4Ti_{16}O_{38}$ crichtonites [22,23]. On the other hand, when Mn^{2+} is replaced by Fe^{2+} (CaMTO *vs.* CaFTO), the expected decrease in *c* lattice parameter ($^{IV}Mn^{2+}$ =0.66 Å, $^{VI}Mn^{2+}$ = 0.83 Å *vs.* $^{IV}Fe^{2+}$ = 0.63 Å, $^{VI}Fe^{2+}$ = 0.78 Å) is again not followed. In this case, two possibilities arise, a 65 % Fe^{2+}/35 % Ti^{3+} *B*1 mixed occupancy or Ca^{2+} fully occupying the *B*1 site instead of Fe thus generating a larger cell volume than CaMTO. Intriguingly, the same happens when comparing LaMTO and LaFTO, after careful refinement it was also found that 0.44 of La^{3+} doping in the *B*1 site. This has also been observed in the crichtonite $La_2Ti_{10.27}Ga_{9.63}O_{38}$ with *B*1 site fully occupied by lanthanum [24]. The effect of Ca replacing Fe on the *B*1 site is clearly reflected in the octahedral bond distances of this site which increase from 2.222(5) Å and 2.2077(1) Å for CaMTO and LaMTO to

Table 1
Cell parameters and BVS for A1 and C3 sites for the different crichtonite compounds. Full crystallographic data is given in supplementary Tables. The data were obtained from Rietveld fitting made to the high-resolution NPD (λ = 1.54 Å) or XRD (λ = 1.54 Å, labelled with an asterisk *) at 293 K.

Compound	Lattice parameters			BVS *A*1	BVS *C*3
	a (Å)	*c* (Å)	Volume (Å^3)		
$CaMn_3(Ti^{4+}_{14}Ti^{3+}_4)O_{38}$ CaMTO	10.4041(2)	20.8157(6)	1951.32(8)	1.36(1)	Ti3 3.61(4)
$CaFe_3(Ti^{4+}_{14}Ti^{3+}_4)O_{38}$ CaFTO	10.3852(1)	20.9221(4)	1954.17(5)	1.34(6)	Ti3/Fe3 [a] 3.7(1)/3.2(1)
$BaMn_3(Ti^{4+}_{14}Ti^{3+}_4)O_{38}$ BaMTO	10.4029(1)	20.8181(4)	1951.10(5)	2.7(1)	Ti1 3.55(3)
$BaMn_3(Ti^{4+}_{14}Fe^{3+}_4)O_{38}$ BaMTFO *	10.4240(5)	20.8400(1)	1961.09(2)	1.70(2)	3.35(6)/3.07(6)
$LaMn_3(Ti^{4+}_{13}Ti^{3+}_5)O_{38}$ LaMTO *	10.4174(1)	20.8206(1)	1956.78(3)	2.05(2)	Ti3 3.07(4)
$LaFe_3(Ti^{4+}_{13}Ti^{3+}_5)O_{38}$ LaFTO *	10.4100(3)	21.0887(8)	1979.16(9)	2.23(2)	Ti3 3.05(5)
$LaMn_3(Ti^{4+}_{13}Fe^{3+}_5)O_{38}$ LaMTFO *	10.4089(1)	20.8052(2)	1952.18(2)	2.61(4)	Fe1 3.13(1)
$CeMn_3(Ti^{4+}_{13}Ti^{3+}_5)O_{38}$ CeMTO *	10.4165(1)	20.8099(1)	1955.42(2)	2.28(2)	Ti3 3.25(6)
$NdMn_3(Ti^{4+}_{13}Ti^{3+}_5)O_{38}$ NdMTO	10.3891(2)	20.7918(6)	1943.49(8)	2.15(1)	Ti3 3.60(1)

[a]Refined site occupancy factors for Ti3/Fe3 were 0.83(1)/0.17(1)%. More details about the refined parameters are shown in Table S1.

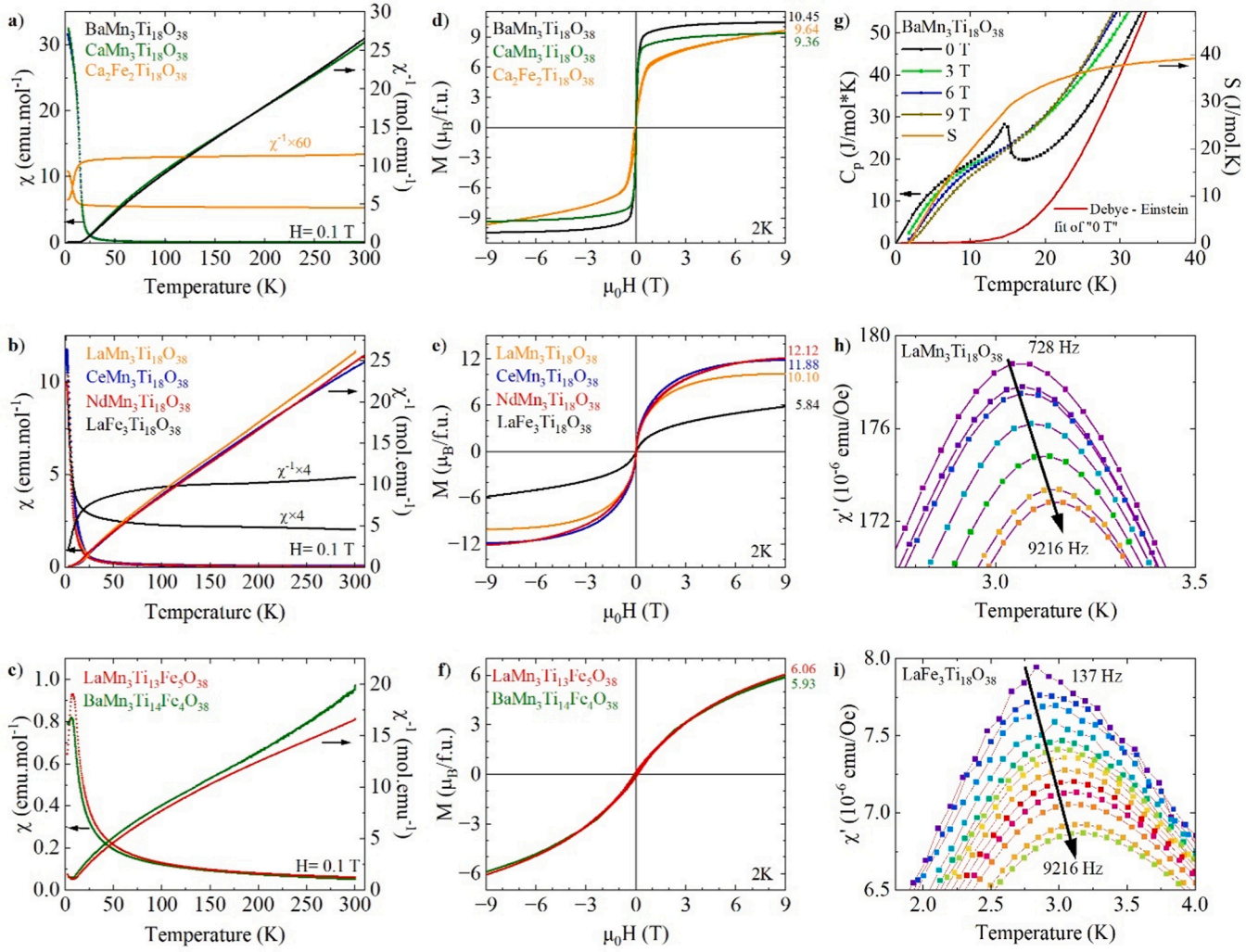

Fig. 2. Magnetic measurements for the crichtonite compounds. a–c) χ(T) and χ^{-1}(T), d-f) M(H) at 2 K, g) C_p for BaMTO and h-i) AC measurements for LaMTO and LaFTO.

Table 2
Magnetic properties of the crichtonite compounds. Curie-Weiss temperature (θ_{CW}), Curie constant (C), effective magnetic moment (μ_{eff}), theoretical magnetic moment (μ_{teo}), $T_{Néel}/T_C$, magnetic moment (MM) observed at 9 T and ideal M_S expected considering FiM alignment between the ions in *B* and *C*3 sites. CaFTO and LaFTO show a Pauli paramagnetic contribution that precluded a proper fit.

Compound	θ_{CW} (K)	C (mol emu^{-1} K^{-1})	μ_{eff} (μ_B/.fu.)	μ_{theo} (μ_B/f.u.)	T_N/T_f (K)	MM at 9 T (μ_B/f.u.)	M_S (μ_B/f.u.)
$CaMn_3Ti_{18}O_{38}$	−7.6(2)	11.8(1)	9.7(2)	10.82[a]	14.4	9.36	11.0
$Ca_2Fe_2Ti_{18}O_{38}$	-	-	-	7.74[b]	6.7	9.64	4.0
$SrMn_3Ti_{18}O_{38}$*	15.0(1)	11.5(1)	9.6(1)	10.82[a]	15.0	10.70	11.0
$SrMn_3(Ti_{14}Fe_4)O_{38}$*	−82.6(4)	21.4(1)	13.1(1)	15.65[c]	8.0	5.80	5.0
$BaMn_3Ti_{18}O_{38}$	3.3(3)	11.2(1)	9.5(3)	10.82[a]	14.8	10.45	11.0
$BaMn_3(Ti_{14}Fe_4)O_{38}$	−11.1(1)	16.0(6)	11.0(1)	15.65[c]	10.5	5.93	5.0
$LaMn_3Ti_{18}O_{38}$	−9.4(1)	11.9(1)	9.8(1)	10.96[d]	4.4	10.10	11.0
$LaMn_3(Ti_{13}Fe_5)O_{38}$	−111.4(2)	24.8(1)	14.1(1)	16.74[e]	12.2	6.06	10.0
$LaFe_3Ti_{18}O_{38}$	-	-	-	9.32[f]	3.5	5.84	8.0
$CeMn_3Ti_{18}O_{38}$	−30.7(2)	13.6(1)	10.4(1)	11.24[g]	3.6	11.88	11.0**
$NdMn_3Ti_{18}O_{38}$	−4.2(1)	12.2(1)	9.9(1)	11.67 [h]	4.0	12.12	11.0**

* from reference [16].
** Without moment from RE.
[a] [3x Mn^{2+} (S = 5/2) + 4xTi^{3+} (S = 1/2)].
[b] [2xFe^{2+} (S = 2)+ 4x Ti^{3+}].
[c] [3xMn^{2+} + 4xFe^{3+} (S = 5/2)].
[d] [3xMn^{3+} + 5xTi^{3+}].
[e] [3xMn^{2+} + 5xFe^{3+}].
[f] [3xFe^{2+} + 5xTi^{3+}].
[g] [1xCe^{3+} (S = ½) + 3xMn^{2+} + 5xTi^{3+}].
[h] [1x Nd^{3+} (S = 3/2)+ 3xMn^{2+}+ 5xTi^{3+}].

2.2793(3) Å and 2.267(1) Å for CaFTO and LaFTO with 100/0 % and 44/56 % Ca/Fe and La/Fe substitution respectively. Ti sites were analyzed through bond valence sum (BVS) calculations, presented in Table S1 and S2. These indicate a predominant Ti^{4+} at *C*1 and *C*2 site, while *C*3 is mixed $Ti^{3+/4+}$ valent in CaMTO, CaFTO, BaMTO and NdMTO crichtonites. On the other hand, a preferential Ti^{3+} at *C*3 site is observed in the remaining compounds: BaMTFO, LaMTO, LaFTO, LaMTFO and CeMTO. This is in agreement with previous reports on BaMTO [9], SrMTO and SrMTFO [9].

In contrast, the cell parameters evolution follows the expected contraction trend when different rare-earths are substituted into AMTO (A = La, Ce and Nd), see Table 1. Finally, in order to study the influence of free *d* electrons increasing in the *C*3 site, $BaMn_3Ti_{14}Fe_4O_{38}$ (BaMTFO) and $LaMn_3Ti_{13}Fe_5O_{38}$ (LaMTFO) were prepared. These should have $4Fe^{3+}$ and $5Fe^{3+}$ instead of their respective Ti^{3+} counterpart in BaMTO and LaMTO. The cell parameters show a decrease due to ionic radii size effects (0.67 and 0.645 Å for Ti^{3+} and Fe^{3+} respectively). A similar behavior was observed for SrMTO and SrMTFO [16]. All these data indicate the introduction of iron into *B* and *C* sites in A-site divalent and trivalent crichtonites and the effect on their magnetic properties is presented below.

DC Magnetic susceptibility measurements for all the compounds are shown in Fig. 2a–c. Their Curie-Weiss behavior at high-temperatures are summarized in Table 2. For CaFTO and LaFTO a Pauli paramagnetic contribution precluded a proper fit, this may be originated from an unknown minority phase, since the expected character for the electrons in these compounds is to be localized. BaMTO, CaMTO and CaFTO show a sharp increase of the magnetic susceptibility below 30 K indicating magnetic transitions at T_N = 14.8(2) K, 14.4(1) K and 6.7(3) K respectively obtained from dχ/dT (Fig. 2a). This increase is less pronounced for RE crichtonites [LaMTO (4.4(1) K), LaFTO (3.5(1) K), CeMTO (3.6(1) K) and NdMTO (4.0(1) K)] and even softer in the crichtonites with iron in the *C*3 sites [BaMTFO (10.5(1) K) and LaMTFO (12.2(1) K)], see Fig. 2b and c. NPD confirmed the ferrimagnetic (FiM) nature of BaMTO, CaMTO and CaFTO transitions as described later.

The calculated effective magnetic moments (μ_{eff}) are slightly reduced from their expected values (μ_{theo}); this could be due to the small amount of secondary phases and thus an error in the considered mass even after corrected or to a reduced fitted range. The field-dependent magnetizations [M(H)] at 2 K for all the compounds are shown in Fig. 2d–f. The M (H) behavior follows the results obtained by the χ(T) measurements: the crichtonites BaMTO, CaMTO and CaFTO along with LaMTO, CeMTO and NdMTO exhibit a more intense response to changes with external field whereas M(H) for BaMTFO, LaFTO and LaMTFO are less sensitive.

BaMTO, CaMTO and CaFTO show an abrupt increase in their magnetic moments at 2 K, reaching 8.9 μ_B, 7.7 μ_B and 5.9 μ_B/f.u., for 0.4 T, 0.3 T and 0.6 T applied fields respectively. Their magnetic moments continue to increase in a slower rate and reach a saturation magnetization (M_s) of 10.5 (BaMTO), 9.4 (CaMTO) and 9.6 μ_B/f.u. (CaFTO) at 9 T. For REMTO (RE = La, Ce and Nd) the initial response is softer and at 9 T they reach 10.1 μ_B/f.u., 11.9 μ_B/f.u. and 12.1 μ_B/f.u. respectively. The remaining BaMTFO, LaMTFO and LFTO crichtonites present a smoother increase with the field, only reaching 5.9 μ_B/f.u. (BaMTFO), 6.1 μ_B/f.u. (LaMTFO), 5.8 μ_B/f.u. (LaFTO), at 9 T. No appreciable hysteresis was found in any of the compounds.

Heat capacity measurements for BaMTO, CaMTO and CaFTO crichtonites are shown in Fig. 2g and SI. Sharp transitions are observed at ~14 K for BaMTO and CaMTO in agreement with T_N observed from χ(T). After subtraction of the lattice contribution (see Fig. S4), the magnetic entropy (S_m) for BaMTO and CaMTO are ~44 and ~40 J mol^{-1} K^{-1} respectively. These values are 65 and 60 % of the theoretical expected value for $S_m = R(3x\ln(2S+1) + 4x\ln(2S+1)) = 67.74$ J mol^{-1} K^{-1} for 3 x Mn^{2+} (S = 5/2) and 4 x Ti^{3+} (S = 1/2), where R = 8.314 J mol^{-1} K^{-1} is the ideal gas constant. On the other hand, CaFTO shows no sharp magnetic transition and S_m = 43.2 J mol^{-1} K^{-1} which is 86.7 % of the expected S_m = 49.81 J mol^{-1} K^{-1} for 2 x Fe^{2+} (S = 5/2) and 4 x Ti^{3+} (S = 1/2). A broad maximum appears in the heat capacity response at low temperatures for CaMTO and BaMTO, as the applied field increases, this moves to higher temperature and diffuses. It is associated to a Schottky anomaly as previously identified in SrMTO [16]. Its contribution follows the relation: $C_{Sch} = NR(\Delta/k_BT)^2 e^{\Delta/k_BT}/(1+e^{\Delta/k_BT})^2$, where Δ is the Schottky gap and k_B is the Boltzmann constant. The BaMTO and CaMTO respective Δ/k_B values are 22.9 K and 29.8 K. Both increased linearly with the magnetic field, see SI, typical of orphan spins or magnetic impurities [25].

The introduction of RE elements in *A* site could also generate new magnetic interactions in the *T* and *T** layers in these compounds, these would interfere with the long-range magnetic order and thus result in a lower T_N or spin-glass phase, as similarly reported in pyrochlore compounds [26,27]. The signatures of non-long-range magnetic order for

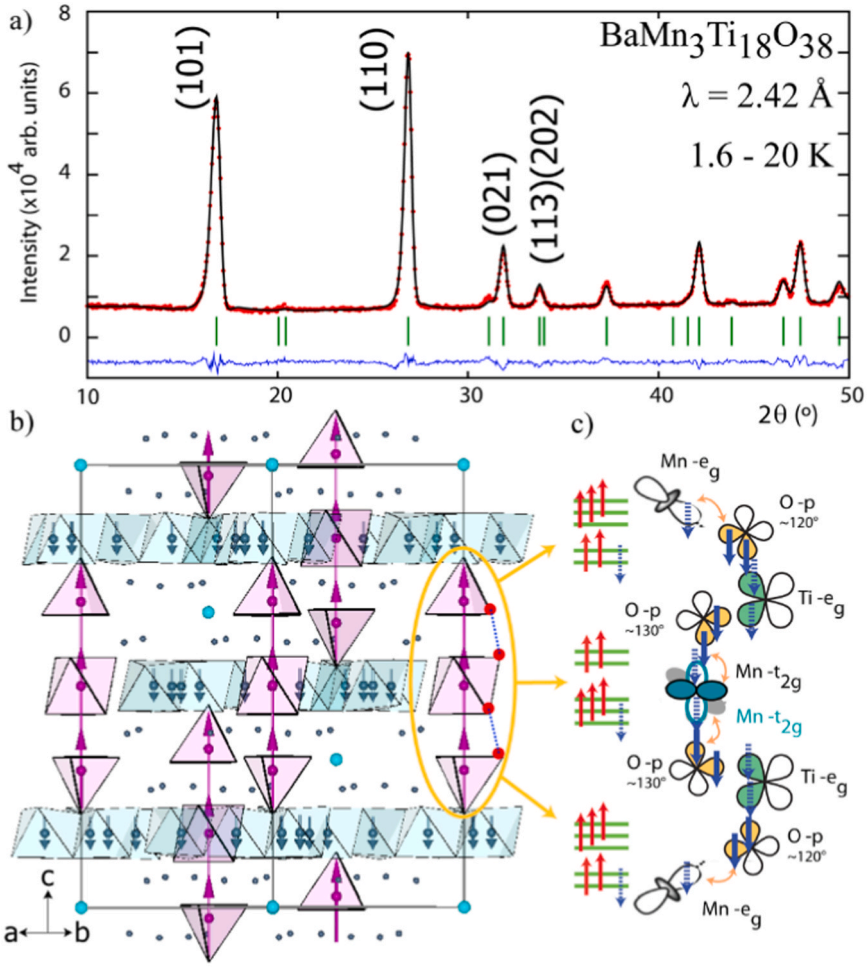

Fig. 3. a) NPD difference at low temperature for BaMTO. b) Magnetic structure with Mn/Ti1 moments in purple/blue. Spheres in cyan/gray represent Ba/Ti. c) Schematic of the Mn($\downarrow e_g$)-O-O-Mn($\downarrow t_{2g}$) ferromagnetic super-super-exchange via Ti^{4+}.

the other six compounds were explored through AC magnetic susceptibility measurements, see Fig. 2h–i, Fig. S3 and Table S4. All these show a frequency (ω) dependence indicating a spin-glass behavior. The freezing temperature (T_f) is properly modeled with the Vogel–Fulcher equation $\omega = \omega_0 \exp\left(\frac{-E_a}{k_B} \bullet (T_f - T_0)\right)$, where $t_0 = \frac{1}{\omega_0}$, E_a and T_0 are the intrinsic relaxation time, the activation energy and Vogel-Fulcher temperature, respectively. Considering the Vogel–Fulcher fits made within the two limits 10^{-13} s $< t_0 < 10^{-9}$ s which are in the interval for spin-glass behaviors [26,27], T_f values do not change more than 0.34 K and activation energies are of the order of 10^{-5} eV when the frequency change four orders of magnitude. The relative shift per frequency decade (δ) was calculated by the relation $\delta_{T_f} = \frac{\Delta T_f}{T_f \Delta \log(\omega)}$ [28,29]. The obtained δ values of 0.022 (LaFTO), 0.010 (BaMTFO), and 0.007 (LaMTO, LaMTFO, CeMTO and NdMTO), indicate a canonical spin-glass for LaFTO, while a FM cluster-glass state for the others with one order of magnitude slower.

Neutron powder diffraction for BaMTO, CaMTO, CaFTO and NdMTO above and below their respective magnetic transitions revealed the appearance of new diffraction maxima for the first three compounds, see Fig. 3 and SI. However, the absence of any extra intensity or new maxima for NdMTO confirmed its spin glass behavior as discussed before. The extra reflections for BaMTO, CaMTO and CaFTO at low temperature establish the long-range magnetic ordering, these were indexed with the same $k_0 = [0\ 0\ 0]$ magnetic propagation vector. Rietveld refinements revealed that the three compounds also follow the same mΓ1 + irreducible representation resulting in the *R-3* (#148.17) magnetic space group. The magnetic structure consists of a ferrimagnetic (FiM) arrangement between parallel Mn^{2+} or Fe^{2+} (*B1* and *B2* sites) aligned along the *z* axis, coupled antiferromagnetically with Ti^{3+} atoms (*C3* site). For BaMTO and CaMTO, the refinement of the magnetic moments in *B1* and *B2* sites were constrained together since they were converging to the same values. On the contrary, for CaFTO, *B1* site is occupied by Ca *i.e.* without a magnetic contribution. The refined magnetic moments at 1.6 K for CaMTO and BaMTO are 3.90(1) μ_B and 4.36(1) μ_B for Mn at *B1* and *B2* sites and 0.17(1) μ_B and 0.24(1) μ_B for Ti at *C3* site, respectively. For CaFTO, the refined magnetic moments are 0.95(3) μ_B for Fe at *B2* site only and 0.22(2) μ_B for Ti at *C3* site. Attempted refinements assuming no magnetic moment in the *C3* site were performed. However, they result in lower quality fits *e.g.* for BaMTO, $\chi^2 = 1.52$ *vs.* 1.85 % and $R_{mag} = 7.67$ *vs.* 8.98 % for considering *vs.* ignoring Ti3 contribution. This *C3* site contribution was also observed in the previously reported SrMTO [16]. Moreover, the M_S from 9 T for BaMTO ($M_S = 10.5\ \mu_B$) and CaMTO ($M_S = 9.4\ \mu_B$) obtained from DC magnetization measurements also support these FiM arrangements since they are close to the ideal value of 11 μ_B by considering 15 μ_B and −4 μ_B coming from the 3xMn^{2+} (S = 5/2) and 4xTi^{3+} (S = 1/2), see Table 2. The difference of M_S values at 9 T between BaMTO and CaMTO comes from the amount of secondary phases found of 6 % and 12.4 %, respectively, and by the 27 % occupancy of Ca at Mn1 site (see Table S1). Also, the different *A* ionic radius induce a bond distance change modifying the orbital overlapping which affects the magnetic interactions. Conversely, for CaFTO, the ideal magnetic moment is calculated to be 4 μ_B considering 8 μ_B and −4 μ_B coming from 2xFe^{2+} (S = 2) and 4xTi^{3+}(S = 1/2), respectively. Nevertheless, one needs to also

Table 3
NPD data.

Sample name		CaMTO	SrMTO*	BaMTO	CaFTO
A-site cation		Ca^{2+}	Sr^{2+}	Ba^{2+}	Ca^{2+}
Ionic radii	(Å)	1.34	1.44	1.61	1.34
Unit cell parameters	*a* (Å)	10.4041 (2)	10.4282 (1)	10.4324 (1)	10.3852(1)
	c (Å)	20.8157 (6)	20.8410 (3)	20.8765 (1)	20.9221(4)
Sample purity	(%)	90.5(5)	97.8(7)	93.9(5)	55.0(2)
Transition temperature	(K)	14.4	14.4	14.8	
Magnetization at 9 T	(μ_B/f. u.)	9.36	10.71	10.45	9.64
Magnetic moments					
Mn1,2	(μ_B)	3.90(1)	4.11(2)	4.36(1)	Fe2–0.95(3)
Ti3	(μ_B)	0.17(1)	0.30(2)	0.24(1)	Ti3/Fe3 – 0.22(2)

* Data taken from Ref. [16].

consider 17 % of iron doping in the *C*3 site, reducing even further the expected moment. Still, the measured M_S for CaFTO (9.6 μ_B) is considerable higher than the ideally expected value in the FiM configuration, this could be due to spin-orbit interactions in Fe^{2+}[30]. The ferromagnetic alignment of the B sites is via *B*1 – O – *C*3 – O – *B*2 super-super-exchange interaction with the help of the Ti^{4+} $3d^0$ linking octahedra, this is schematically shown in Fig. 3c. Ferromagnetic super-super exchange has been observed in CrI_3 layers via Cr – I – Te – Fe [31] electron hopping or in a similar tetrahedra – octahedra – tetrahedra motif in $Ba_5Co_5FO_{13}$ [32,33]. The thermal evolution of the Mn and Ti magnetic moments in BaMTO are shown in SI. Mn moment is properly modeled by the critical law $\mu(T) = \mu_0[1 - (T/T_N)]^{\beta}$ with $\mu_0 = 4.4(1)$ μ_B, $T_N = 14.7(1)$ K and $\beta = 0.36(3)$, related to a 3D Heisenberg magnet. Fully unsaturated magnetic Mn moments have also been reported in the double perovskite Mn_2FeReO_6 (3.5 μ_B), in the $LiNbO_3$-type $MnTiO_3$-II (3.9 μ_B) [34,35] and in the crichtonite SrMTO (4.4 μ_B) [16]. (Table 3).

Summarizing, we have successfully synthesized nine new members of the $AB_3C_{18}O_{38}$ crichtonite family. They all crystallize in their typical rhombohedral structure with space group *R*-3. Stoichiometric compositions were obtained for most of the materials except for CaMTO, CaFTO and LaFTO, in which Ca doped 15 % and 100 % and La 44 % on the *B*1 site, respectively. Long-range magnetic ordering at low temperatures was only found for the divalent crichtonites BaMTO, CaMTO and CaFTO with $T_N = 14.8$, 14.4 and 6.7 K respectively. The change from a ferrimagnetic spin arrangement to spin-glass behavior in the studied crichtonites was determined to be due to: 1) cation disorder between Ti and Fe in the *C*3 site, as observed from BaMTO (FiM) to BaMTFO (spin-glass) and 2) introduction of competing interactions via RE substitution into the A site. This work sheds light over the potential of divalent crichtonites over those containing rare earths elements, thus marking the line to follow in future research.

CRediT authorship contribution statement

Marie Colmont: Writing – review & editing, Supervision. **Oleg Siidra:** Writing – review & editing, Supervision. **Angel M. Arevalo-Lopez:** Writing – review & editing, Supervision, Conceptualization. **Claire Minaud:** Formal analysis, Data curation. **Clemens Ritter:** Writing – review & editing, Methodology, Formal analysis. **Jose Luis Rosas-Huerta:** Methodology, Formal analysis, Data curation. **Ruiqi Chen:** Writing – review & editing, Formal analysis.

Declaration of Competing Interest

The authors declare that they have no known competing financial interests or personal relationships that could have appeared to influence the work reported in this paper.

Acknowledgments

We thank the ILL for beamtime provided at D20 (DOI:https://doi.org/10.5291/ILL-DATA.5-31–2921). J. L. R. H. thanks the SECTEI/098/2022-Mexico and SECIHTI for the post-doctoral fellowships. R. C. thanks Region Hauts-de-France for a Ph.D. scholarship. The Chevreul Institute (FR 2638), Region Hauts-de-France, and FEDER are acknowledged for funding the X-ray diffractometers and the PPMS magnetometer.

Appendix A. Supporting information

Supplementary data associated with this article can be found in the online version at doi:10.1016/j.jallcom.2025.182889.

References

[1] R.J.D. Tilley, Perovskites: Structure-Property relationships, Wiley, 2016.
[2] R.H. Mitchell, Perovskites: Modern and Ancient, Almax Press, 2002.
[3] N.S. Arul, V.D. Nithya, Revolution of Perovskite, Springer, 2020.
[4] L. Zhang, Q. Zhou, Q. He, T. He, Double-perovskites $a_2FeMoO_{6-\delta}$ (*a* = Ca, Sr, Ba) *as anodes* for solid oxide fuel cells, J. Power Sources 195 (2010) 6356–6366.
[5] C. Ritter, M.R. Ibarra, L. Morellon, J. Blasco, J. García, J.M.De Teresa, Structural and magnetic properties of double perovskites AA'$FeMoO_6$ (AA' = Ba_2, BaSr, Sr_2 and Ca_2), J. Phys. Condens. Matter 12 (2000) 8295–8308.
[6] P. Kayser, A. Muñoz, J.L. Martínez, F. Fauth, M.T. Fernández-Díaz, J.A. Alonso, Enhancing the Néel temperature in 3d/5d R_2NiIrO_6 (R=La, Pr and Nd) double perovskites by reducing the R^{3+} ionic radii, Acta Mater. 207 (2021) 116684.
[7] T.H. Green, N.J. Pearson, High-pressure, synthetic loveringite-davidite and its rare earth element geochemistry, Mineral. Mag. 51 (1987) 145–149.
[8] B.M. Gatehouse, I.E. Grey, I.H. Campbell, P. Kelly, The crystal structure of loveringite, a new member of the crichtonite group, Am. Miner. 63 (1–2) (1978) 28–36.
[9] R.C. Peterson, I.E. Grey, Preparation and structure refinement of synthetic Ti^{3+}-containing lindslevite $BaMn_3Ti_{18}O_{38}$, Can. Miner. 33 (5) (1995) 1083–1089.
[10] R.K. Rastsvetaeva, S.M. Aksenov, N.V. Chukanov, L.A.D. Menezes, Crystal structure of almeidaite, a new mineral of the crichtonite group, Dokl. Chem. 455 (2014) 53–57.
[11] L.A.D. Menezes Filho, N.V. Chukanov, R.K. Rastsvetaeva, S.M. Aksenov, I.V. Pekov, M.L.S.C. Chaves, R.P. Richards, D. Atencio, P.R.G. Brandao, R. Scholz, K. Krambrock, R.L. Moreira, F.S. Guimaraes, A.W. Romano, A.C. Persiano, L.C. A. de Oliveira, J.D. Ardisson, Almeidaite, $Pb(Mn,Y)Zn_2(Ti,Fe^{3+})_{18}O_{36}(O,OH)_2$, a new crichtonite-group mineral, from novo horizonte, bahia, Brazil, Mineral. Mag. 79 (2) (2015) 269–283.
[12] P.-A. Wülser, N. Meisser, J. Brugger, K. Schenk, S. Ansermet, M. Bonin, F. Bussy, Cleusonite, $(Pb,Sr)(U^{4+},U^{6+})(Fe^{2+},Zn)_2(Ti,Fe^{2+},Fe^{3+})_{18}(O,OH)_{38}$, a new mineral species of the crichtonite group from the Western Swiss Alps, Eur. J. Miner. 17 (6) (2006) 933–942.
[13] V. Butvina, A. Spivak, T. Setkova, O. Safonov, High-Pressure synthesis, synchrotron Single-Crystal XRD and Raman spectroscopy of synthetic K–Ba minerals of magnetoplumbite, crichtonite and hollandite group indicatory of mantle metasomatism, Minerals 13 (2) (2023) 192.
[14] W.L. Gong, R.C. Ewing, L.M. Wang, H.S. Xie, Crichtonite structure type ($Am_{21}O_{38}$ and $A_2M_{19}O_{36}$) as a host phase in crystalline waste form ceramics, MRS Online Proc. Libr 353 (1994) 807–815.
[15] T.M. Smith Pellizzeri, C.D. McMillen, Y. Wen, G. Chumanov, J.W. Kolis, Iron vanadates synthesized from hydrothermal brines: $Rb_2FeV_6O_{16}$, $Cs_2FeV_6O_{16}$, and $SrFe_3V_{18}O_{38}$, Eur. J. Inor. Chem. 42 (2019) 4486–4604.
[16] J.L. Rosas-Huerta, R. Chen, C. Ritter, O. Siidra, M. Colmont, A.M. Arévalo-López, Ferrimagnetic and spin glass behaviour in $SrMn_3^{2+}Ti_{14}^{4+}M_4^{3+}O_{38}$ (M = Ti and Fe) synthetic crichtonites, Chem. Commun. 59 (2023) 13199–13202.
[17] B.J. Campbell, H.T. Stokes, D.E. Tanner, D.M. Hatch, ISODISPLACE: a web-based tool for exploring structural distortions, J. Appl. Crystallogr. 39 (4) (2006) 607–614.
[18] J. Rodriguez-Carvajal, Recent advances in magnetic structure determination by neutron powder diffraction, J. Phys. Condens. Matter 192 (1993) 55–69.
[19] J. Rodriguez-Carvajal, T. Roisnel, FullProf.98 and WinPLOTR: new Windows 95/NT applications for diffraction commission for powder diffraction, IUCR Newsl. No 20 (1998).
[20] R.R.K Rastsvetaeva, Crichtonite and its family: the story of the discovery of two new minerals, Miner. Crystallogr 8 (2020) 39–47.
[21] P. Wülser, N. Meisser, The crichtonite group of minerals: a review of the classification, Bull. Liaison S. F. M. C. 16 (2004) 76–77.
[22] B.M. Gatehouse, I.E. Grey, The crystal structure of $Ca_2Zn_4Ti_{16}O_{38}$, J. Solid State Chem. 46 (1983) 151–155.
[23] R.C. Peterson, I.E. Grey, L.M.D. Cranswick, C. Li, The stability and crystal chemistry of synthetic loveringite in the system Ca-Mn-Ti-O under strongly reducing conditions, Can. Miner. 36 (1998) 763–774.

[24] A. Meden, D. Kolar, S. Škapin, Crystal structure and powder data of davidite-type $La_2Ti_{10.27}Ga_{9.63}O_{38}$, Powder Diffr. 14 (1999) 36–41.
[25] T. Zhu, B. Zhu, O. Mentré, S. Lee, D. Chen, Y. Jin, W. Zhu, A.M. Arévalo-López, C. Minaud, K.Y. Choi, M. Lu, $Cu_3Te_2O_5(OH)_4$: a frustrated Two-Dimensional quantum "Magnetic Raft" as a possible pathway to a spin liquid, Chem. Mater. 35 (2023) 3951.
[26] K. Binder, A.P. Young, Spin glasses: experimental facts, theoretical concepts and open questions, Rev. Mod. Phys. 58 (1986) 801.
[27] O.G. Ellert, A.V. Egorysheva, Unusual magnetic properties of ternary Bi- and Ln-containing pyrochlores: from cooperative paramagnetism to canted antiferromagnetism and reentrant spin glass, Pyrochlore Ceram. 315 (2022).
[28] N. Marcano, P.A. Algarabel, L.F. Barquín, J.P. Araujo, A.M. Pereira, J.H. Belo, C. Magén, L. Morellón, M.R. Ibarra, Cluster-glass dynamics of the griffiths phase in $Tb_{5-x}LaxSi2Ge_2$, Phys. Rev. B 99 (2019) 054419.
[29] T. Klimczuk, H.W. Zandbergen, Q. Huang, T.M. McQueen, F. Ronning, B. Kusz, J. D. Thompson, R.J. Cava, Cluster-glass behavior of a highly oxygen deficient perovskite, $BaBi_{0.28}Co_{0.72}O_{2.2}$, J. Phys. Condens. Matter 21 (2009) 105801.
[30] S. Mugiraneza, A.M. Hallas, Tutorial: a beginner's guide to interpreting magnetic susceptibility data with the Curie-Weiss law, Commun. Phys. 5 (2022) 95.
[31] Y. Zhao, S. Zhou, J. Zhao, Enhanced intralayer ferromagnetism in CrI_3 by interfacial Super-Superexchange interaction, J. Phys. Chem. C 126 (2022) 17306–17312.
[32] O. Mentré, M. Kauffmann, G. Ehora, S. Daviero-Minaud, F. Abraham, P. Roussel, Structure, dimensionality and magnetism of new cobalt oxyhalides, Solid State Sci. 10 (2008) 471–475.
[33] G. Ehora, C. Renard, S. Daviero-Minaud, O. Mentré, New $BaCoO_{3-\delta}$ polytypes by rational substitution of O^{2-} for F^-, Chem. Mater. 19 (2007) 2924–2926.
[34] A.M. Arevalo-Lopez, G. McNally, J.P. Attfield, Large magnetization and frustration switching of magnetoresistance in the Double-Perovskite ferrimagnet Mn_2FeReO_6, Angew. Chem. Int. Ed. 54 (2015) 12074–12077.
[35] A.M. Arevalo-Lopez, J.P. Attfield, Weak ferromagnetism and domain effects in multiferroic $LiNbO_3$-type $MnTiO_3$-II, Phys. Rev. B 88 (2013) 104416.